Chemical Science

EDGE ARTICLE

View Article Online
View Journal

Check for updates

Cite this: DOI: 10.1039/d5sc03646a

All publication charges for this article have been paid for by the Royal Society of Chemistry

Received 20th May 2025
Accepted 26th June 2025

DOI: 10.1039/d5sc03646a

rsc.li/chemical-science

A dynamic amphiphilic additive with dual solubility modulates Zn^{2+} solvation and *in situ* SEI for a dendrite-free zinc anode†

Can-Fei Xiao,[a] Yong-Xia Lu,[a] Ming Lu,[a] Dongxiang Luo,[a] Kang Xiao,*[a] Yongke Wang[c] and Zhao-Qing Liu*[ab]

Aqueous zinc-ion batteries (AZIBs) have garnered significant attention due to their inherent safety and cost-effectiveness, with electrolyte additives playing a pivotal role in enhancing their electrochemical performance. However, the current research landscape reveals a notable gap in the exploration of colloidal additives for AZIB electrolyte systems. This study addresses this limitation by introducing a novel colloidal electrolyte system comprising two synergistic components: a dissolved fraction that modulates the Zn^{2+} solvation structure through small molecules, and an insoluble colloidal fraction that facilitates the formation of a robust solid-electrolyte interphase (SEI) at the anode surface. We propose the innovative use of perylene-3,4,9,10-tetracarboxylic acid diimide (PTCDI) as a multifunctional colloidal additive to engineer a hybrid electrolyte with weak solvation effects. The PTCDI additive demonstrates unique multisite zincophilicity and hydrophobicity, effectively reducing free water content and nucleation potential within the hydrogen bonding network, thereby promoting uniform zinc nucleation. This innovative approach yields remarkable electrochemical performance, achieving stable zinc stripping/plating for 2800 hours with a minimal overpotential of 58.4 mV and an exceptional coulombic efficiency of 99.94%. Zn||MnO_2 full cells with a low negative/positive electrode capacity ratio of 9.5 exhibit stable cycling performance, maintaining functionality over 500 cycles at a current density of 1 A g^{-1} at −30 °C. These findings establish colloidal additives as a promising paradigm for advancing AZIB electrolyte design, offering new insights into the development of high-performance zinc-ion battery systems.

Introduction

The growing demand for clean and sustainable energy has driven extensive research into electrochemical energy storage systems.[1–4] Among various energy storage technologies, AZIBs have emerged as particularly promising candidates for stationary storage and micropower applications, primarily due to their unique combination of advantages: low cost, inherent safety, and high theoretical capacity (820 mA h g^{-1}).[5–7] However, the practical implementation of AZIBs faces significant challenges stemming from the complex interfacial chemistry of zinc anodes in aqueous electrolytes. These challenges manifest in several detrimental phenomena, including zinc dendrite formation, the hydrogen evolution reaction (HER), and the accumulation of passive by-products, all of which severely compromise the reversibility of zinc deposition/stripping processes and ultimately lead to battery performance degradation.[8] A critical aspect of these issues lies in the coordination environment of Zn^{2+}, particularly the solvation sheath structure, which plays a pivotal role in the electrochemical processes occurring at the anode/electrolyte interface during charging. Addressing these challenges requires a dual-focused approach: precise regulation of the Zn^{2+} solvation structure and strategic design of the zinc anode interface, both of which are essential for developing high-performance, durable AZIBs suitable for practical applications.

Significant progress has been made in developing modification strategies to enhance the interfacial compatibility between zinc electrodes and aqueous electrolytes, with current approaches primarily focusing on surface coating,[9,10] structure engineering,[11] and electrolyte optimization.[12] While surface coating and structural engineering methods have demonstrated some effectiveness, they often involve complex fabrication processes that increase production costs and introduce inactive components that compromise the overall energy density of the batteries. Electrolyte optimization has emerged as a more straightforward and promising approach for improving zinc

---

[a] School of Chemistry and Chemical Engineering, Institute of Clean Energy and Materials, Guangzhou Key Laboratory for Clean Energy and Materials, Guangzhou University, Guangzhou 510006, China. E-mail: kxiao@gzhu.edu.cn; lzqgzhu@gzhu.edu.c

[b] School of Chemistry, South China Normal University, Guangzhou 510006, China

[c] Engineering Department, University of Miami, Miami 32812, USA

† Electronic supplementary information (ESI) available. See DOI: https://doi.org/10.1039/d5sc03646a

anode–electrolyte compatibility.[13] Recent advancements in electrolyte engineering have primarily focused on three key strategies: the development of co-solvent systems, highly concentrated electrolytes, and the incorporation of electrolyte additives. Highly concentrated electrolytes, in particular, have shown potential in modifying the Zn^{2+} solvation structure and reducing water activity in the solvation sheath, thereby mitigating water-induced parasitic reactions. However, these systems face significant limitations, including increased electrolyte viscosity that impedes charge transfer, elevated desolvation barriers leading to high voltage polarization, and substantial production costs that hinder large-scale manufacturing. These challenges highlight the need for innovative electrolyte design strategies that can simultaneously address multiple performance limitations while maintaining cost-effectiveness for practical applications in AZIBs.

The strategic incorporation of trace electrolyte additives has emerged as a transformative approach to enhance the electrochemical performance of AZIBs.[14–17] These additives can be systematically classified into three categories based on their solubility characteristics: completely soluble additives (CSAs), partially soluble additives (PSAs) and completely insoluble additives (CIAs). Nowadays, CSAs play a leading role in electrolyte additives, such as metal salts, organic small molecules, polymers, and natural organic compounds.[18–21] In the aqueous electrolyte, CSAs are a sort of free molecule or ion that frequently alters the surface of AZIBs through sacrificial breakdown or molecular absorption, as well as the solvation structure of Zn^{2+} ions. In contrast, CIAs represent an emerging class of additives, typically comprising solid nanomaterials such as nanoparticles or nanosheets suspended in the electrolyte.[22–24] These insoluble additives operate through distinct mechanisms, participating in Zn^{2+} coordination and facilitating the *in situ* formation of dynamic SEI *via* electrostatic adsorption or precipitation reactions. However, the inherent limitations of both approaches are becoming increasingly apparent. CIAs, while effective in SEI formation, exhibit minimal impact on Zn^{2+} solvation structure due to their insoluble nature. Conversely, CSAs, despite their effectiveness in solvation structure modification, often fail to form robust SEI layers due to their limited molecular adsorption thickness. In order to incorporate the benefits of both CSAs and CIAs, a new class of electrolyte additives is expected to be developed. This fundamental trade-off between solvation structure control and SEI formation highlights the need for innovative additive designs that can synergistically combine the benefits of both approaches. Beyond solubility considerations, the molecular architecture of additives, particularly the nature and arrangement of functional groups, plays a crucial role in determining electrochemical performance. Current research has predominantly focused on hydroxyl-rich additives such as glycerol and ethylene glycol, which leverage extensive hydrogen bonding networks to modulate electrolyte structure. However, these systems present significant limitations: the formation of extended molecular chains through "hand-in-hand" hydrogen bonding leads to increased electrolyte viscosity, which in turn impedes Zn^{2+} mobility and compromises ionic conductivity. These viscosity-related challenges manifest as poor rate capability and limited cycle life, underscoring the need for alternative molecular designs.[25,26]

Herein, we present an effective approach to address the multifaceted challenges in AZIBs, through the strategic implementation of PTCDI as a multifunctional, amphiphilic additive. This innovative design achieves a "Multiple Birds with One Stone" effect, simultaneously enhancing zinc anode stability and electrolyte performance across a wide temperature range. Our strategy integrates two key components: (1) propylene carbonate (PC) as a co-solvent to create a mixed electrolyte system, and (2) PTCDI as a PSA that exists in a dynamic equilibrium between CIA and CSA states. The unique dual-phase nature of PTCDI enables distinct yet complementary functions: the insoluble colloidal fraction forms a robust, durable SEI layer on the zinc anode surface, while the soluble molecular component effectively modulates the Zn^{2+} solvation structure. From a molecular design perspective, PTCDI represents a significant departure from traditional hydroxyl-rich additives. Its carbonyl groups, characterized by inherent electronegativity and strong binding affinity with zinc,[27,28] enable specific adsorption at the electrode–electrolyte interface. This molecular architecture provides three critical advantages: (1) significant reduction of interfacial water content,[29] (2) disruption of hydrogen bonding networks, and (3) decrease in free water proportion. These effects collectively contribute to enhanced electrochemical performance and extended operational temperature range. These exceptional outcomes also extend to workable anode-free zinc metal batteries (AFZMBs), which display extraordinary stability. Electrochemical studies and characterizations confirmed that PTCDI improved the stability of Zn plating/stripping by encouraging de-solvation, the development of a molecular adsorption layer, and the prevention of side reactions. This work will broaden the design philosophy of anti-freezing electrolytes and promote wide temperature large-scale energy storage adopting aqueous batteries.

Results and discussion

As a polycyclic aromatic organic molecule, PTCDI features excellent electron transport capability and stable chemical properties. Given its insolubility in water and limited solubility in PC, the saturated concentration of PTCDI in 30% PC aqueous solution is approximately 5 mM. In addition, flammability tests confirmed that the 30% PC electrolyte retains the high-safety merit of aqueous electrolytes (Fig. S1†). In the PSA system, PTCDI above the saturated concentration exists as a colloid. A 10 mM PTCDI solution was prepared using a mixed electrolyte of water and PC (denoted as $Zn(OTf)_2$/PC + PTCDI). Within this $Zn(OTf)_2$/PC + PTCDI system, the dissolved PTCDI can penetrate the solvated sheath layer, while the colloidal PTCDI specifically adsorbs onto the Zn anode. Optical testing further confirmed the colloidal nature of the system. Specifically, in comparison with the other two groups, the $Zn(OTf)_2$/PC + PTCDI exhibits a distinct optical path, providing evidence of the colloidal state within the system (Fig. S2†). Zn deposition is comprehensively illustrated in Scheme 1a. The notorious interfacial chemical

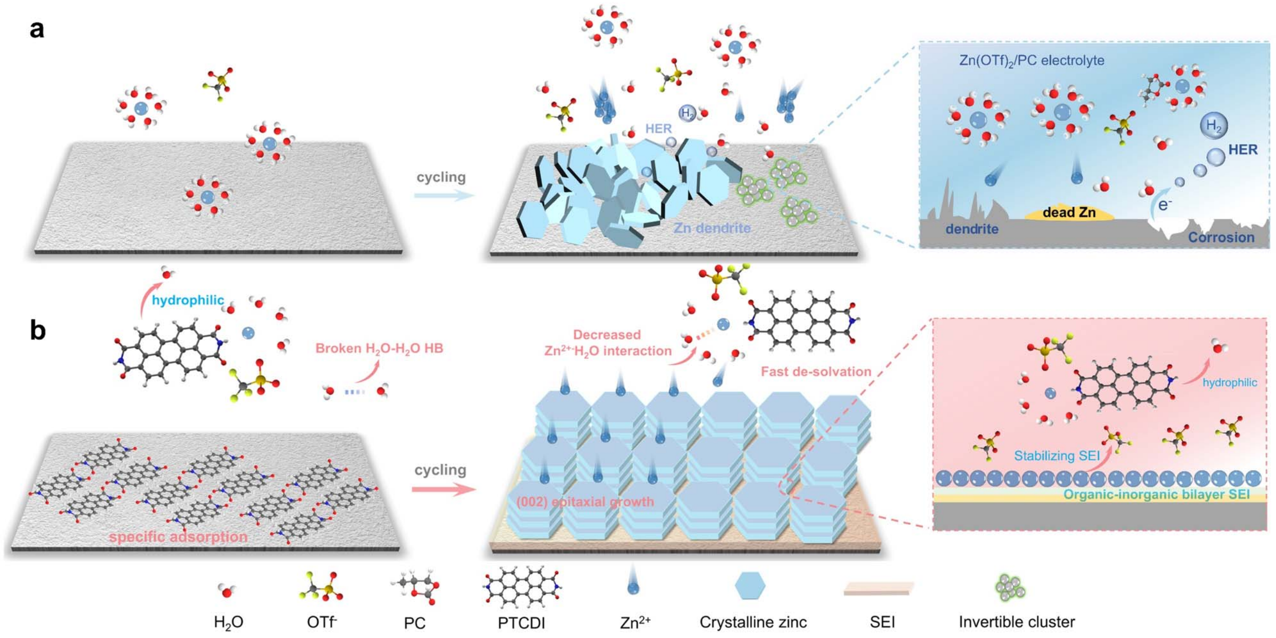

Scheme 1 Schematic illustration of the Zn surface evolution. (a) Schematic diagram of Zn dendrites and HER in Zn(OTf)$_2$/PC electrolyte. (b) The mechanism for enhancing zinc electrode stability by PTCDI additive.

properties of the zinc anode in aqueous electrolytes, including dendrite growth, HER, and by-product accumulation, seriously restrict the reversibility of zinc anode deposition and stripping, which causes the performance of full batteries to substantially deteriorate. Reducing the de-solvation energy barrier by additives through pre-desolvation helps to mitigate side reactions, and the reduced energy barrier accelerates the kinetics of Zn nucleation and facilitates uniform Zn deposition. As illustrated in Scheme 1b, PTCDI regulates zinc deposition in the batteries by altering the solvation structure. In Zn(OTf)$_2$/PC electrolyte, abundant and highly polar water molecules dominate the primary solvation shell of Zn^{2+},leading to a high de-solvation energy barrier. This process could lead the coordinated water to protonate and even cause side reactions on the electrode surface including corrosion and insoluble precipitation. Nevertheless, PTCDI displaces the water molecules from the solvated sheath layer of Zn^{2+}, forming a new solvated structure. More importantly, PTCDI also helps anions to enter the solvated sheath layer as it replaces water molecules, creating a "weak solvation" structure. During the Zn^{2+} deposition, an *in situ* SEI composed of ZnF_2 forms, promoting the formation of Zn (002) planes and inhibiting dendrite formation.[30] To demonstrate the influence of PTCDI molecules participating in the solvation structure of Zn^{2+} on the interfacial chemical properties of the Zn anode, the highest occupied molecular orbital (HOMO) and the lowest unoccupied molecular orbital (LUMO) for free H_2O and PTCDI were calculated *via* density functional theory (DFT) based on first-principles calculations.

As depicted in Fig. 1a, PTCDI exhibits a higher energy level of the highest HOMO relative to that of H_2O (-6.372 eV *vs.* -8.148 eV). This implies that upon adsorption of PTCDI on the surface of the Zn foil, it is more prone to donate electrons.[31] Moreover, in the vicinity of the anode surface, the relatively lower LUMO of PTCDI predisposes it to undergo electrochemical reactions and decomposition preferentially. Consequently, the stronger interaction between PTCDI and the surrounding species impels PTCDI to be incorporated into the solvation shell of Zn^{2+} by displacing the coordinated water molecules. This process facilitates the preferential reduction and decomposition of anions on the surface of the Zn anode, leading to the formation of an inorganic-rich SEI. The influence of PTCDI molecules on Zn nucleation was investigated by analyzing the electrophilic and nucleophilic active sites using the molecular electrostatic potential (MESP) method. As shown in Fig. 1b, the red-colored regions denote negative MESP values (nucleophilic centers), while the blue-colored regions represent positive MESP values (electrophilic centers). These results suggest that the carbonyl group in PTCDI demonstrates electronegativity, acting as an active site for the capture of zinc ions during the nucleation process. The molecular structure of PTCDI is presented in Fig. S3.† Given that the benzene ring backbone of PTCDI exhibits hydrophobic properties, while the carbonyl groups display zincophilicity, PTCDI can be classified as an amphiphilic molecule. CV was performed to demonstrate that PTCDI has no redox activity in the electrolyte. The CV curves of two electrolytes with and without PTCDI added are basically similar, which is attributed to zinc electrochemistry and water decomposition (Fig. S4†). This experimental conclusion is consistent with PTCDI's molecular structure: the perylene diimide core lacks conventional aqueous redox activity within this potential range. Quantum chemical calculations were carried out to explore the interaction characteristics among Zn^{2+} ions, PC, and PTCDI molecules. PTCDI features a significant number of highly polar carbonyl groups. Owing to the presence of

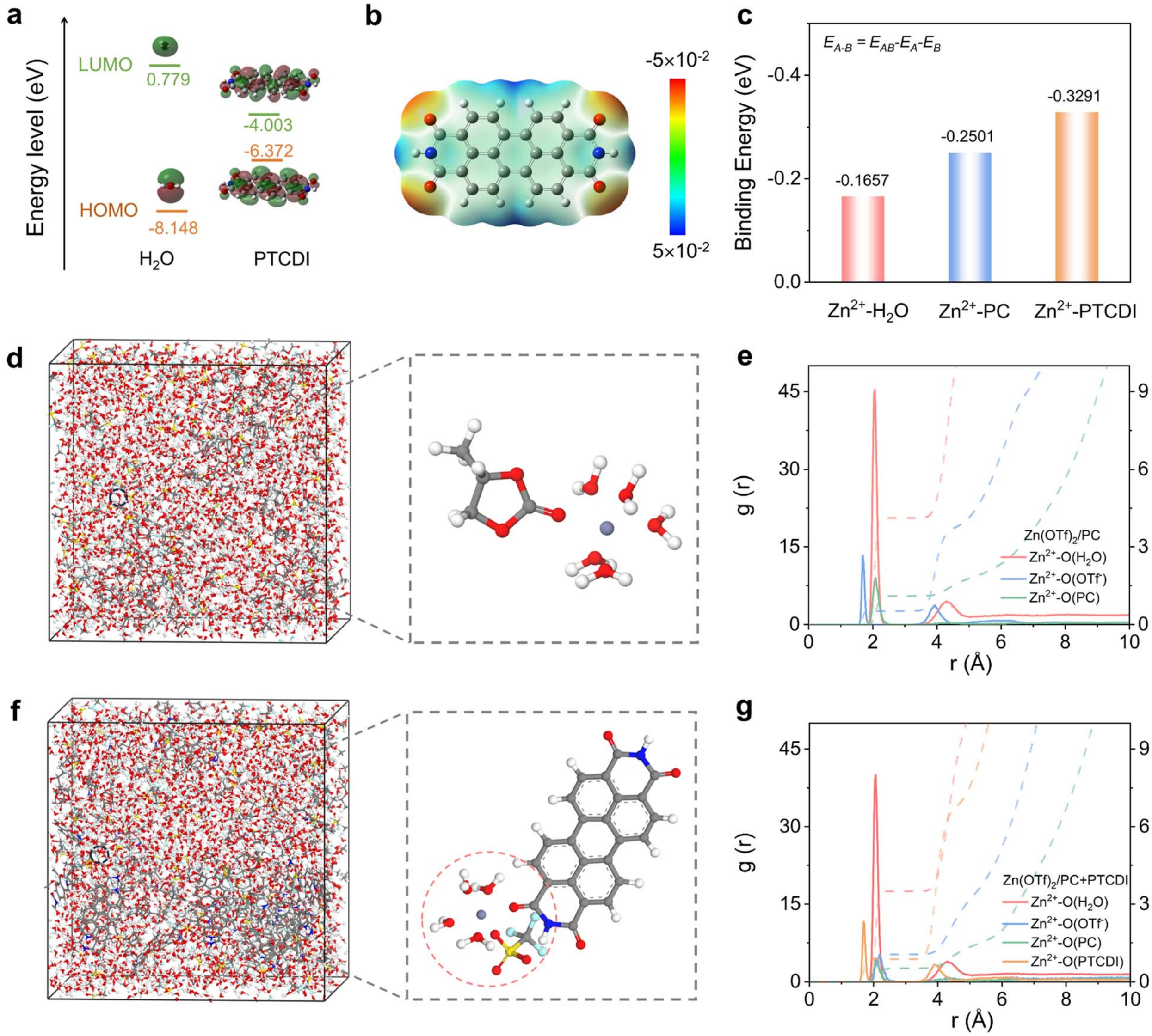

Fig. 1 Theoretical calculations. (a) HOMO–LUMO energy levels with corresponding isosurfaces of free H_2O and PTCDI. (b) MESP diagram of PTCDI. (c) Binding energy of different solvent Zn^{2+} pairs. 3D snapshot of (d) $Zn(OTf)_2$/PC and (f) $Zn(OTf)_2$/PC + PTCDI obtained from MD simulations and partial enlarged snapshots representing Zn^{2+} inner solvation structures. The corresponding radial distribution function plots for (e) $Zn(OTf)_2$/PC and (g) $Zn(OTf)_2$/PC + PTCDI.

unsaturated double bonds, these carbonyl groups possess a greater reducing capacity compared to hydroxyl groups. As depicted in Fig. 1c, the binding energy between PTCDI molecules and Zn^{2+} (−0.3091 eV) is stronger than that between PC and Zn^{2+} (−0.2501 eV) and that between H_2O and Zn^{2+} (−0.1657 eV). This indicates a more favorable interaction between PTCDI and Zn^{2+}. The strong binding energy of PTCDI with Zn means that the de-solvation process of hydrated Zn^{2+} at the new electric double layer is much easier than in the $Zn(OTf)_2$/PC electrolyte, which helps to accelerate the transfer of hydrated Zn^{2+} at the interface. Moreover, upon the introduction of PTCDI, the presence of adsorbed PTCDI on the surface serves to hinder dendrite growth, while the flat anode surface diminishes the concentration gradient near the anode, leading to accelerated ion diffusion. These combined influences collectively expedite the transfer of hydrated Zn^{2+} at the interface. The results indicate that Zn^{2+} prefers binding to the PTCDI over H_2O to form a new solvation structure of Zn ions, which aligns with the previous MESP results. In addition, the electric double-layer capacitance (EDLC) value of the Zn electrode in $Zn(OTf)_2$/PC + PTCDI is 166.03 μF cm^{-2}, larger than that in $Zn(OTf)_2$/PC (157.97 μF cm^{-2}), indicating the adsorption between the Zn electrode and PTCDI is stronger than that between the Zn electrode and OTf^- (Fig. S5†).[32]

Molecular dynamics (MD) simulations were subsequently performed to analyze the solvation sheath structure of $Zn(OTf)_2$/H_2O, $Zn(OTf)_2$/PC and $Zn(OTf)_2$/PC + PTCDI systems. OTf^- ions were introduced into the solvated system to simulate the natural environment better. The computational results suggest that upon complete stabilization within a pure $Zn(OTf)_2$

environment, the primary solvation sheath (PSS) of Zn^{2+} comprises $5H_2O$ molecules and $1OTf^-$ ion (Fig. S6†). As depicted in Fig. 1d, the incorporation of PC is capable of substituting a water molecule within the solvated sheath layer of Zn^{2+}. The addition of PTCDI effectively diminishes the desolvation energy barrier by replacing $2H_2O$ in the inner solvation sheath, thereby exerting a notable influence on the relevant electrochemical processes (Fig. 1e). The introduction of PTCDI into the electrolyte results in the substitution of one H_2O molecule in the PSS with a single PTCDI (Fig. 1f). Reduced water in the inner solvation sheath of the hydrated zinc ion and increased Zn^{2+} desolvation would result from the PTCDI and Zn^{2+} having a strong enough connection to replace one or more water molecules in the zinc hexahydrate ion $[Zn(H_2O)_6]^{2+}$. The corresponding radial distribution functions and coordination number analysis were derived from the calculated results in various electrolyte models. In the $Zn(OTf)_2/H_2O$ electrolyte, the peak observed in the Zn–O pair at ≈2.1 Å away from Zn^{2+} can be attributed to the presence of H_2O molecules in the PSS. The sharp peak observed in the Zn–O pair at ≈1.84 Å away from Zn^{2+} should be attributed to the presence of OTf^- ions in the solvation structure. Comparably, in the $Zn(OTf)_2$/PC + PTCDI system (Fig. 1g), the peak of Zn–O derived from OTf^- and H_2O still appeared at ≈1.84 and 1.94 Å. The peak of Zn–O originating from PTCDI appears at ≈2.21 Å from Zn^{2+}, implying some PTCDI molecules enter into the PSS. In addition, the average coordination numbers of Zn–O (H_2O) in PSS shift from 4.42 in pure $Zn(OTf)_2$/PC electrolytes to 4.25 within $Zn(OTf)_2$/PC + PTCDI electrolytes. This observation indicates that the introduction of PTCDI has the capacity to regulate the number of coordinated water molecules. Concurrently, the coordination number of OTf^- within the system comprising PTCDI increases from 1.58 to 1.44, thus substantiating the regulatory influence exerted by PTCDI. Simultaneously, molecular dynamics (MD) simulations were employed to quantify the number of hydrogen bonds between H_2O molecules in the $Zn(OTf)_2$/PC + PTCDI electrolyte. The results revealed a notable decrease compared to the $Zn(OTf)_2$/PC and $Zn(OTf)_2/H_2O$ electrolytes (Fig. S7†). This finding further corroborates that PTCDI exerts a regulatory effect on the initial hydrogen bond network of active water molecules through its carbonyl functional groups, consequently reconstructing a stable hydrogen bond network. This reconstructed network restricts the mobility of water molecules, leading to a decrease in the electrolyte's freezing point and the HER.

Linear sweep voltammetry (LSV) curves were initially obtained to verify the stable voltage window of the electrolytes. In the $Zn(OTf)_2$/PC + PTCDI electrolyte, the presence of large hydrophobic groups in PTCDI disrupts the original hydrogen bond network and decreases the proportion of free water molecules. As a result, the HER potential in this electrolyte is measured to be only −81 mV, which is significantly lower than those observed in the $Zn(OTf)_2$/PC and $Zn(OTf)_2/H_2O$ electrolytes (Fig. 2a). Additionally, the LSV curves for the oxygen evolution reaction (OER) confirm that the $Zn(OTf)_2$/PC + PTCDI electrolyte exhibits a higher potential. These results indicate that Zn foils exhibit a reduced corrosion tendency in the $Zn(OTf)_2$/PC + PTCDI electrolyte (Fig. S8†). The voltage distribution of the zinc nucleation stage is shown in Fig. 2b. The PTCDI electrolyte has a smaller overpotential (−58.4 mV) compared with the PC electrolyte (−138.8 mV), which proves that PTCDI can reduce the nucleation barrier during Zn deposition.[33] Nuclear magnetic resonance was used to further examine the solvation structures of different electrolytes (Fig. 2c). The ability of additives to combine with Zn^{2+} is reflected in the shift of the signal towards the high field.[34] The combination of electron-donating carbonyl groups in the PTCDI additive with Zn^{2+} causes the H resonance signal in $Zn(OTf)_2$/PC + PTCDI to shift up-field, increasing the electron density around water molecules and improving shielding. The upfield shift reflects the ability of additives to coordinate with Zn^{2+}. Typically, the deposition of hydrated Zn^{2+} on the Zn electrode surface involves three steps, including liquid phase transport, de-solvation and solid phase transport on the electrode surface.[35] Taking advantage of the fast ionic transport in the aqueous electrolyte and the passivation-free Zn surface constructed by PTCDI, the energy barriers for liquid-phase transport and electrode surface solid-phase transport can be neglected compared to the de-solvation process. Therefore, the de-solvation of hydrated Zn^{2+} approximates the Arrhenius activation energy (E_a).[36] The results obtained from the Arrhenius equation indicate that the desolvation activation energy of $Zn(OTf)_2$/PC + PTCDI is 29.75 kJ mol^{-1} lower than that of $Zn(OTf)_2$/PC (66.82 kJ mol^{-1}) (Fig. 2d, e and S9†). This suggests that PTCDI facilitates the removal of water from $Zn(H_2O)_6{}^{2+}$ and enhances the deposition kinetics.

Moreover, the introduction of PTCDI also alters the hydrogen bond network. The wide O–H stretching vibration peak observed in the Raman spectra of Fig. 2f, within the range of 2800 cm^{-1} to 3800 cm^{-1}, can be divided into two peaks at 3232.2 cm^{-1} and 3552.7 cm^{-1}. These peaks can be classified as strong and weak hydrogen bonds, respectively.[37] Upon the introduction of PC and PTCDI, the relative intensity of the strong hydrogen bond peak increases while that of the weak H-bond peak decreases. This phenomenon suggests that PC and PTCDI incorporate into the solvation shell of Zn^{2+},[38] a result that is in agreement with previous theoretical calculations. Intuitively, the proportion of weak hydrogen bonds in the $Zn(OTf)_2$/PC + PTCDI electrolyte is evidently lower than that in the $Zn(OTf)_2$/PC electrolyte, which further demonstrates that PTCDI is effective in breaking the hydrogen bond between H_2O molecules. Additionally, the O–H stretching bands of H_2O in the $Zn(OTf)_2$/PC + PTCDI electrolyte exhibit a positive shift, providing further evidence that the original hydrogen bond network is interrupted upon the introduction of PTCDI (Fig. S10†). Furthermore, $Zn(OTf)_2$/PC + PTCDI exhibits better rate performance than $Zn(OTf)_2$/PC symmetric cells. As shown in Fig. 2g and h, despite the poor mass transfer processes due to the viscosity of organic solvents, the $Zn(OTf)_2$/PC + PTCDI electrolyte shows relatively high ion transport numbers (0.919) relative to the $Zn(OTf)_2$/PC systems (0.830) (Fig. S11†). Additionally, chronoamperometry (CA) tests conducted at −150 mV were employed to assess the impact of the PTCDI additive on zinc nucleation and growth. The continuous and rampant

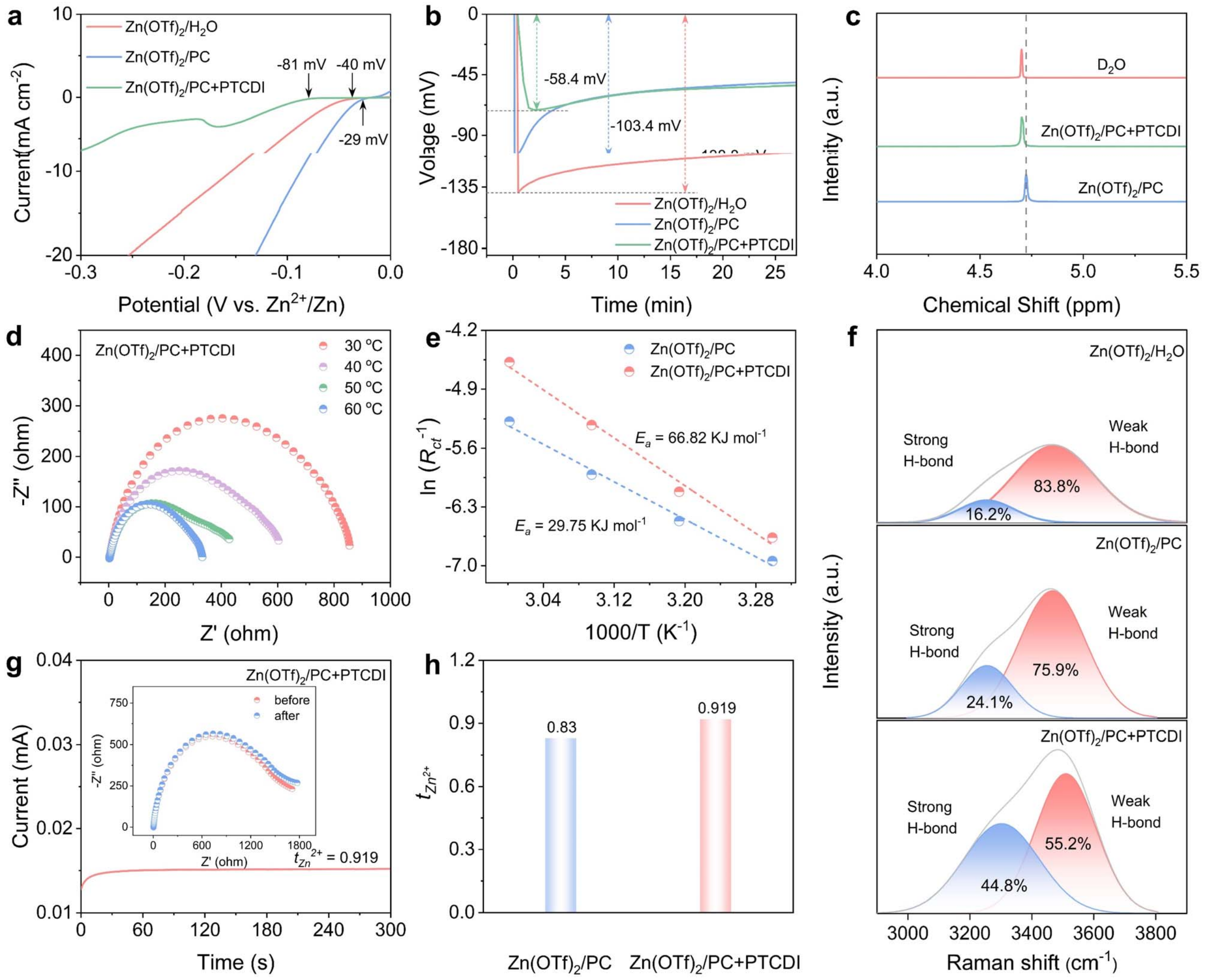

Fig. 2 Electrochemical and morphological characterizations of the Zn anodes. (a) LSV curves of asymmetric Zn‖Ti cells in various electrolytes. (b) Nucleation overpotential of asymmetrical cells. (c) ^1H NMR spectra in different electrolytes. (d) Nyquist plots of $Zn(OTf)_2$/PC + PTCDI electrolyte at different temperatures. (e) Arrhenius plots of ln(1/*R*) *vs.* 1000/*T* for the zinc electrode in $Zn(OTf)_2$/PC and $Zn(OTf)_2$/PC + PTCDI electrolytes. (f) Raman spectra of different electrolytes in the range of 3000–3800 cm^{-1}. (g) CA plots and the EIS spectra before/after polarization (inset) of Zn‖Zn cells in $Zn(OTf)_2$/PC + PTCDI electrolyte. (h) Zn ion transport numbers.

horizontal two-dimensional diffusion process of Zn^{2+} along the Zn surface, seeking favorable nucleation sites to minimize surface energy, is evidenced by the continual current density drops observed in the $Zn(OTf)_2$/PC electrolyte (Fig. S12†).[39,40] This phenomenon suggests that the prolonged 3D diffusion process in the $Zn(OTf)_2$/PC + PTCDI electrolyte facilitates the mitigation of Zn dendrite formation.

In order to gain insight into the composition and structure of the SEI formed by $Zn(OTf)_2$/PC + PTCDI, X-ray photoelectron spectroscopy (XPS) and transmission electron microscopy (TEM) were employed. The SEI on the Zn anode after 20 cycles was analyzed under conditions of a current density of 1 mA cm^{-2} and a discharge capacity of 1 mA h cm^{-2}. The EDS mapping (Fig. S13†) and spectra (Fig. S14†) confirmed that the primary constituent elements of the SEI are C, F, and S derived from OTf^- anions. The TEM images show the ZnF_2, $ZnCO_3$, and ZnS crystals with distinct lattice structures in the inner phase of the SEI, revealing the presence of the inorganic crystalline rich inner phase of the SEI after Zn plating (Fig. 3a–f). This suggests that on the zinc electrode, an organic–inorganic hybrid ZnF_2–ZnS-rich interface was generated *in situ*. It should be noted that the ZnF_2–ZnS-rich contact shields the zinc surface from water and inhibits parasitic reactions while enabling strong Zn^{2+} conductivity.[41] The chemical composition of the interfacial layer on the cycled Zn surface with $Zn(OTf)_2$/PC and $Zn(OTf)_2$/PC + PTCDI electrolytes was analyzed using XPS. The increase in ZnF_2 and ZnS observed in the $Zn(OTf)_2$/PC + PTCDI electrolyte compared to $Zn(OTf)_2$/PC indicates the *in situ* formation of an organic–inorganic hybrid ZnF_2–ZnS-rich interface on the zinc electrode (Fig. 3g, h, S15a and b†). It is noteworthy that the presence of electronegative F can facilitate the *in situ* generation of ZnF_2 on the Zn anode surface.[42] This process induces Zn(002) orientation deposition, which serves to inhibit the growth of dendrites. The F 1s spectra indicated that the peak could be

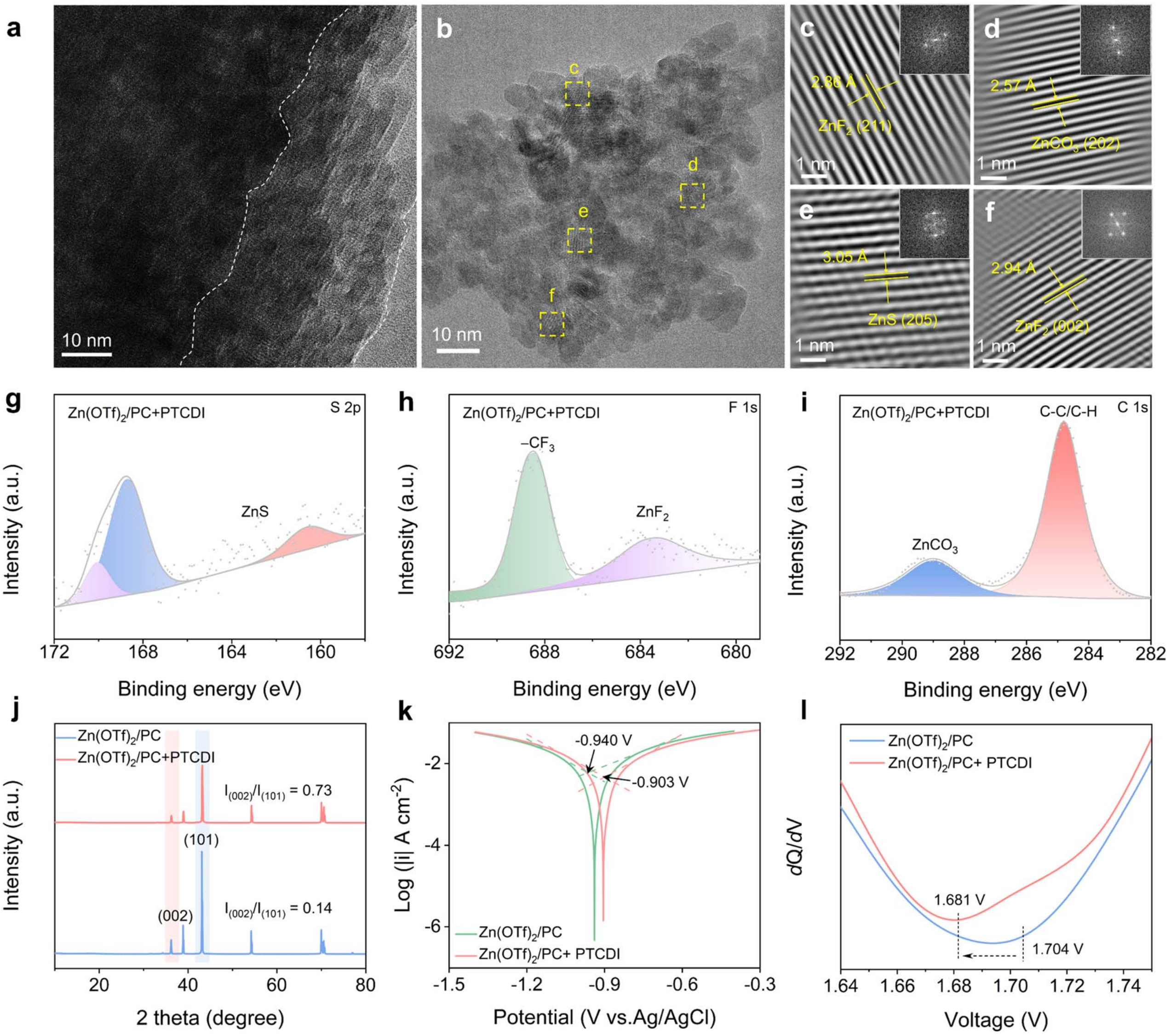

Fig. 3 Experimental characterizations for SEI characterization on the Zn anode. (a–f) TEM images of the SEI formed in Zn(OTf)$_2$/PC + PTCDI electrolyte. XPS characterization of the SEI. XPS spectra of (g) S 2p and (h) F 1s of the Zn foil cycled in Zn(OTf)$_2$/PC + PTCDI electrolyte. (i) XPS spectra of the Zn electrode surface with Zn(OTf)$_2$/PC + PTCDI electrolyte. (j) XRD patterns of Zn foil after 100 cycles of plating/stripping. (k) Linear polarization curves of the Zn anode in Zn(OTf)$_2$/PC and Zn(OTf)$_2$/PC + PTCDI electrolytes. (l) Differential capacitance potential curves for the copper (Cu) electrode in Zn(OTf)$_2$/PC and Zn(OTf)$_2$/PC + PTCDI electrolytes.

deconvoluted into inorganic ZnF$_2$ and organic –CF$_3$. The preceding analysis demonstrates that the SEI is constituted of organic and inorganic components, including ZnF$_2$ and ZnS.[43] This is advantageous for the homogeneous deposition of Zn metal and the inhibition of side reactions.[44] An organic/inorganic composite SEI forms at the electrode/electrolyte interface. The inorganic layer exhibits excellent ionic conductivity, while the organic layer demonstrates good flexibility, enabling effective coping with volume changes due to dendrite growth. This special SEI layer improves the performance of high-rate and long-cycle batteries by facilitating Zn^{2+} conduction, preventing direct contact between the electrolyte and the Zn electrode, inhibiting dendritic development, and lowering the likelihood of numerous side reactions. Moreover, the intensity of the peak in the C 1s spectra is markedly reduced in the presence of PTCDI. ZnCO$_3$ is widely understood to be a by-product of parasitic reactions (HER and associated corrosion) at the interface.[45] The significant suppression of ZnCO$_3$ formation with PTCDI provides further corroborating evidence that PTCDI effectively mitigates these detrimental side reactions (Fig. 3i and S15c†). Furthermore, the Zn anode's contact angle was measured in order to examine its hydrophilicity. The reduced contact angle in the Zn(OTf)$_2$ electrolyte suggests that the Zn surface becomes more hydrophilic upon plating. This results from the rough and porous layer of zinc plating. The Zn anode's wettability may be improved by the more hydrophilic surface, but it also makes the side reactions easier.[46] However, as seen by the wide contact angle (103.25°), a far more hydrophobic surface can be achieved in the Zn(OTf)$_2$/PC + PTCDI electrolyte (Fig. S16†).

To effectively prevent the interaction between the active zinc and water, a hydrophobic surface of this kind is essential for creating a confined water-poor environment in the inner Helmholtz layer. In the Zn metallic feature, the (002) plane's hexagonal arrangement shows less surface energy than the (101) plane.[47] Therefore, the higher values of $I_{(002)}/I_{(101)}$ dictate the uniformity of Zn deposition. As illustrated in Fig. 3j, the Zn cycled in $Zn(OTf)_2$/PC + PTCDI exhibits a much higher intensity ratio of Zn(002) to Zn(101) than that in the $Zn(OTf)_2$/PC electrolyte (0.73 *vs.* 0.14). According to the Tafel curve, the Zn electrode's corrosion current density in the $Zn(OTf)_2$/PC electrolyte is 8.08 mA cm^{-2}, and its corrosion potential is −0.940 V. In contrast, the $Zn(OTf)_2$/PC + PTCDI electrolyte exhibits a corrosion potential of −0.903 V and a corrosion current density of 7.14 mA cm^{-2}. These findings suggest that the corrosion reaction is significantly inhibited by the presence of PTCDI (Fig. 3k and S17†). To determine adsorption behavior, alternating current voltage measurement was also used, with a range of 1.64–1.75 V. Fig. 3l illustrates how the addition of PTCDI causes a negative shift in the potential of zero charge, which stands for the minimum capacitance. This change results from PTCDI molecules' specific adsorption on the Zn electrode surface, which promotes the formation of nucleation sites and the induction of homogeneous deposition.

Leveraging the bifunctional impact of PTCDI greatly improved the stability and reversibility of the Zn plating–stripping process. Zn‖Zn cells with the PTCDI additive can maintain stability for over 2800 h, much longer than those without the PTCDI additive (Fig. 4a). The remarkable stability can be ascribed to the incorporation of PTCDI. PTCDI serves to lower

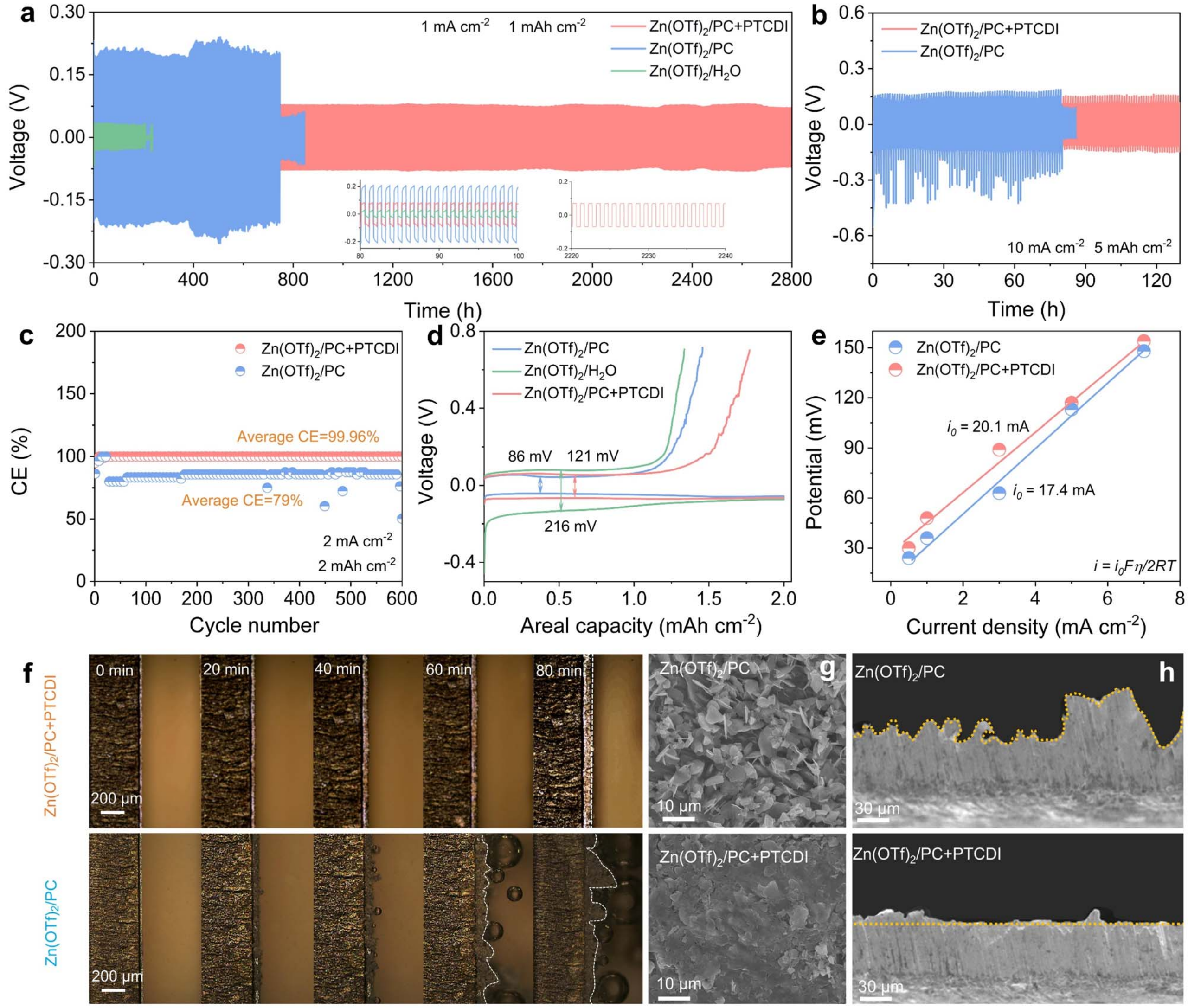

Fig. 4 Electrochemical reversibility and stability of the Zn foil anode. Voltage profiles of Zn symmetric cells assembled with $Zn(OTf)_2$/PC + PTCDI electrolytes at current densities of (a) 0.5 mA cm^{-2} and (b) 10 mA cm^{-2}. (c) The CE of Zn‖Ti cells in $Zn(OTf)_2$/PC electrolytes with and without PTCDI at 2 mA cm^{-2} and 2 mA h cm^{-2}. (d) The initial discharge/charge voltage gap. (e) Exchange current density calculated from curves obtained at different current densities in Zn symmetric cells. (f) *In situ* optical microscopy images of the cross-sectional Zn plating morphology on the Zn anode in $Zn(OTf)_2$/PC + PTCDI (above) and $Zn(OTf)_2$/PC (below). (g) SEM images of plated Zn cycled 100 times. (h) Cross-sectional SEM images of cycled Zn electrodes of the Zn‖Zn cells with $Zn(OTf)_2$/PC and $Zn(OTf)_2$/PC + PTCDI electrolytes for 100 cycles.

the desolvation energy barrier of Zn^{2+} and curtail the HER. Concurrently, it leads to a decrease in by-products on the Zn electrode. These combined effects result in a substantial reduction of voltage hysteresis and a notable attenuation of voltage fluctuations. However, In the $Zn(OTf)_2$/PC, a significant voltage hysteresis is observed. This phenomenon can be ascribed to two primary factors: the elevated desolvation energy associated with hydrated Zn^{2+} and the copious byproducts generated on the surface of the Zn anode. These factors play crucial roles in governing the observed behavior, with the high desolvation energy of hydrated Zn^{2+} presenting a significant kinetic barrier, while the large amounts of byproducts on the Zn anode surface can impede electrode processes and influence overall system performance. What's more, the cells in $Zn(OTf)_2$/PC + PTCDI can still run stably with a high current density for more than 120 h (Fig. 4b). The improved migratory capacity of Zn^{2+} ions and the efficient suppression of dendritic development are attributed to the high CE and prolonged cycle life. The result reveals that the $Zn(OTf)_2$/PC + PTCDI electrolyte can withstand a maximum current density of 16 mA cm^{-2} at 10 mA h cm^{-2}, while the $Zn(OTf)_2$/PC electrolyte exhibits a short-circuit. The Zn‖Ti half-cells were assembled to examine the CE of the cell operation. Compared with the $Zn(OTf)_2$/PC electrolyte, which has an average CE of 79%, the $Zn(OTf)_2$/PC + PTCDI electrolyte has a higher average CE of 99.6% (Fig. 4c). Furthermore, the polarization voltage also exhibits a significant variation during cycling. The initial voltage hysteresis (~121 mV) for $Zn(OTf)_2$/PC + PTCDI (Fig. 4d) is significantly smaller than that of $Zn(OTf)_2$/PC (~216 mV), suggesting a reduced potential barrier for Zn plating/stripping.

In addition, the reversible property of Zn symmetric cells at various current densities was evaluated to assess their practicality. The $Zn(OTf)_2$/PC exhibits a higher overpotential throughout the process and experiences voltage fluctuation upon returning to 1 mA cm^{-2} (Fig. S18†). To evaluate the interfacial transfer kinetics, the exchange current density (i_0) is computed from the overpotential (η) at various current densities. When compared to $Zn(OTf)_2$/PC (17.4 mA), Fig. 4e demonstrates that $Zn(OTf)_2$/PC + PTCDI gives the highest i_0 value of 20.1 mA, indicating a greatly enhanced charge transfer capability that can support smooth Zn deposition. *In situ* optical vision measurements confirmed the existence of zinc anode plating in both electrolytes. For the $Zn(OTf)_2$/PC + PTCDI based cell, uniform and compact zinc deposition was achieved at a current density of 2 mA cm^{-2}. As expected, after 60 minutes of deposition, significant bubble formation and visible dendrites were observed on the surface of the zinc foil in the $Zn(OTf)_2$/PC electrolyte (Fig. 4f). The post-cycling surface morphology of the electrodes was examined using SEM. The cycled Zn electrode in the $Zn(OTf)_2$/PC electrolyte exhibited a rough and uneven surface. This is attributed to the inhomogeneous electric field distribution and tip effect, which caused rapid vertical growth of deposited zinc particles, resulting in a disordered cone-shaped dendrite structure (Fig. 4g and S19†). In contrast, the Zn electrode cycled in the $Zn(OTf)_2$/PC + PTCDI electrolyte showed a smooth and flat surface (Fig. 4g and h). Moreover, Zn foils were immersed into two electrolytes for 7 d at room temperature. The noticeable difference is that the surface of Zn foil in $Zn(OTf)_2$/PC + PTCDI electrolyte is compact and smooth while the Zn foil in $Zn(OTf)_2$/PC electrolyte develops a lump-covered corrosion layer (Fig. S20†). PTCDI significantly disrupts the original hydrogen bond network and establishes strong electrostatic interactions with dipolar water molecules, thereby modulating hydrogen bonds and controlling the freezing point of water.[48] The tolerance at low temperatures was contrasted with that of the electrolyte $Zn(OTf)_2/H_2O$. The $Zn(OTf)_2$/PC + PTCDI electrolyte maintains good liquidity down to −30 °C, while the aqueous electrolyte solidifies at −20 °C (Fig. S21†). In addition, we performed a comparative analysis of the cycling stability performance of Zn‖Zn symmetric cells using different electrolytes and operating at low temperatures. Under conditions of a constant voltage hysteresis at a current density of 1 mA cm^{-2} and an areal capacity of 1 mA h cm^{-2} per cycle, the $Zn(OTf)_2$/PC + PTCDI electrolyte exhibited significantly enhanced longevity (exceeding 1000 h compared to 280 h) at −30 °C (Fig. 5a). The Zn‖Ti half-cells were assembled to examine the CE of the cell operation. Compared with the $Zn(OTf)_2$/PC electrolyte, which has an average CE of 57.3%, the $Zn(OTf)_2$/PC + PTCDI electrolyte has a higher average CE of 97.6% (Fig. 5b). A full AZIB is constructed with Zn as the anode and MnO_2 as the cathode to evaluate the potential applications of the $Zn(OTf)_2$/PC + PTCDI electrolyte.

The CV curve displays two distinct redox peaks, suggesting that the incorporation of PTCDI molecules does not adversely affect the redox reactions at the MnO_2 cathode.[49] As shown in Fig. S22,† the cathodic peak at 1.32 V disappears when $Zn(OTf)_2$ is omitted from the electrolyte, suggesting that only the dissolution/deposition process occurs in $Mn(OTf)_2$ + PTCDI electrolyte. Additionally, pure $Mn(OTf)_2$ exhibits a very weak current response, demonstrating that PTCDI significantly enhances the dissolution/deposition kinetics of MnO_2/Mn^{2+}.[50] Additionally, $Zn(OTf)_2$/PC + PTCDI electrolyte has a lower voltage gap between redox peaks than $Zn(OTf)_2$/PC electrolyte, which suggests less polarization and faster transfer kinetics (Fig. S23†). The galvanostatic charge–discharge (GCD) curves provide further confirmation of this result. In particular, the GCD curves of the $Zn(OTf)_2$/PC + PTCDI electrolyte illustrate its improved symmetry and capacity compared to that of the $Zn(OTf)_2$/PC electrolyte due to the superior ionic conductivity and optimized solvation structure (Fig. S24†). A reasonable negative-to-positive electrode ratio (N/P) is of critical importance for the rigorous practical application of AZIBs. We fabricated a Zn‖MnO_2 full battery featuring a 50 μm Zn anode coupled with high-mass-loading MnO_2 cathodes (up to 10 mg cm^{-2}), yielding N/P ratios of 9.5 to assess electrochemical performance under high Zn anode utilization. After 800 cycles at a current density of 2 A g^{-1}, AZIBs with $Zn(OTf)_2$/PC + PTCDI electrolyte demonstrate a high capacity of ≈170 mA h g^{-1} (Fig. S25†), which is significantly higher than that of $Zn(OTf)_2$/PC (140 mA h g^{-1}). Moreover, the XRD spectra indicate that the PTCDI additive is capable of suppressing the formation of $Zn_xOTf_y(OH)_{2x-y}\cdot H_2O$ on the electrode surface (Fig. S26†). This suppression enhances the ionic transport and charge transfer processes that occur during the reaction. Similarly, the cycle

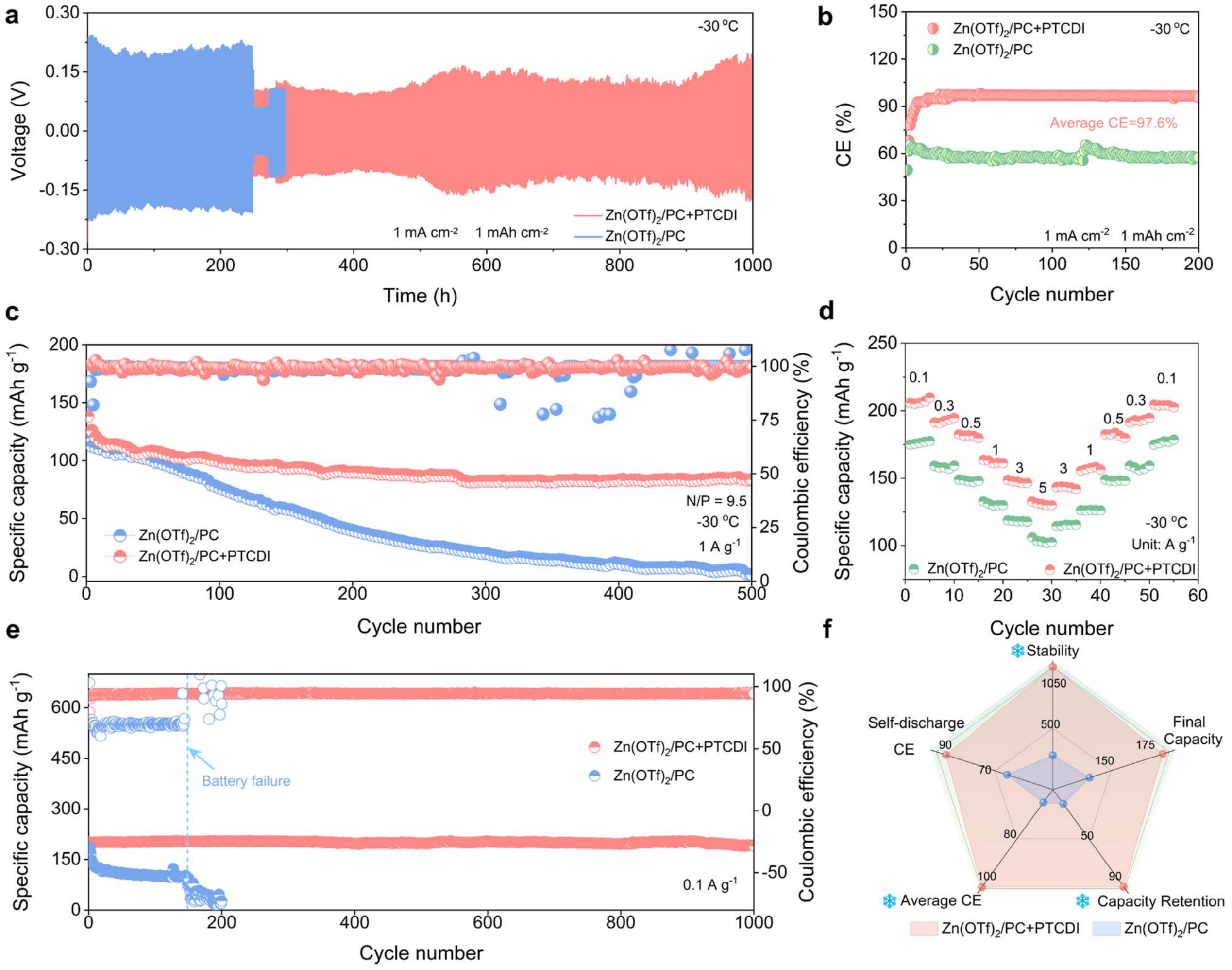

Fig. 5 Electrochemical performance of full cells and anode free Cu||$ZnMn_2O_4$ batteries. (a) Voltage profiles of Zn symmetric cells assembled with $Zn(OTf)_2$/PC + PTCDI electrolytes at −30 °C. (b) The CE of Zn||Ti cells in $Zn(OTf)_2$/PC electrolytes with/without PTCDI at −30 °C. (c) Long cycling stability performance of the Zn||MnO_2 full cell in $Zn(OTf)_2$/PC and $Zn(OTf)_2$/PC + PTCDI electrolytes at −30 °C. (d) Rate performance of the Zn||MnO_2 full cell in $Zn(OTf)_2$/PC and $Zn(OTf)_2$/PC + PTCDI electrolytes at −30 °C. (e) Cycling performance of anode-free Cu||$ZnMn_2O_4$ batteries. (f) Performance comparison of Zn||MnO_2 cells in $Zn(OTf)_2$/PC and $Zn(OTf)_2$/PC + PTCDI electrolytes.

stability at −30 °C was further studied (Fig. 5c). However, $Zn(OTf)_2$/PC based AZIBs suffer from rapid battery failure under the same conditions. This suggests its immense potential for low temperature applications, a testament to the robust stability conferred by PTCDI with its enhanced Zn^{2+} transport ability, superior anti-freezing properties, and a stable electrolyte/electrode interface. Electrochemical impedance spectroscopy (EIS) was also used to examine the impact of the PTCDI additive on the interfacial impedance of the Zn||MnO_2 complete cells (Fig. S27†). The semicircle in the middle-frequency area of the EIS shrinks after the PTCDI additive is added, suggesting that the impedance of H^+ and Zn^{2+} flowing through the electrode surface's insulating layer is reduced. According to the rate performance curves at −30 °C (Fig. 5d), AZIBs with $Zn(OTf)_2$/PC + PTCDI electrolyte have greater capacity over a range of current densities than those with $Zn(OTf)_2$/PC electrolyte. This suggests that the PTCDI molecules provide excellent low-temperature performance for Zn. Additionally, the storage capabilities of Zn||MnO_2 with $Zn(OTf)_2$/PC and $Zn(OTf)_2$/PC + PTCDI electrolyte were assessed. The completely charged Zn||MnO_2 cell was released after a 24 hour storage period. The impact of PTCDI on adverse responses was assessed using capacity retention. The CE of the second cycle following the quiescence for the $Zn(OTf)_2$/PC + PTCDI electrolyte stayed at 83.3%, while the $Zn(OTf)_2$/PC complete cell value was only 65.6% (Fig. S28†).

In addition to the full cell, we evaluated the viability of the $Zn(OTf)_2$/PC + PTCDI electrolyte in AFZMBs, where devices were constructed using $ZnMn_2O_4$ as the cathode material and Cu foil as the anode negative collector. As shown in Fig. 5e, the Cu||$ZnMn_2O_4$ battery using $Zn(OTf)_2$/PC + PTCDI electrolyte exhibits excellent cycling stability. After 1000 cycles, a high capacity of 200 mA h g^{-1} remains, corresponding to the CE of approximately 94.8%. In contrast, the rapid capacity decay observed in the AFZMB using the $Zn(OTf)_2$/PC electrolyte after 180 cycles can be attributed to the limited zinc supplement (zero excess zinc). The advantages of the $Zn(OTf)_2$/PC + PTCDI electrolyte are further substantiated by its effective performance in AFZMBs. A radar plot comparing the overall performance of the two electrolytes clearly shows that the PTCDI-modified electrolyte significantly outperforms the PC-only electrolyte, validating the success of the modification strategy (Fig. 5f and S29†).

Conclusions

In summary, we present a PTCDI-based colloidal electrolyte with improved performance in AZIBs. The amphiphilic nature of PTCDI enables dual functionality: its soluble components help regulate the Zn^{2+} solvation structure, while the insoluble colloidal particles contribute to the formation of a stable SEI layer on the zinc anode. Experimental results combined with DFT calculations suggest that PTCDI promotes the formation of (002) crystalline surfaces, which helps reduce nucleation overpotential and provides more active sites for zinc deposition. The hydrophobic properties of PTCDI, along with its ability to reduce free water content, effectively suppress side reactions in the electrolyte. The optimized electrolyte system shows promising performance: Zn symmetric cells achieve stable cycling for 2800 hours at 1 mA cm^{-2}/1 mA h cm^{-2} at room temperature, and maintain operation for 1000 h at −30 °C. This work provides a potential direction for developing cost-effective electrolyte additives, which could help address some of the challenges currently limiting the practical application of AZIBs.

Data availability

All the data supporting this article have been included in the main text and the ESI.†

Author contributions

Z. L. and K. X. conceived and supervised the research, acquired funding, and contributed to writing – review & editing. C. X. conducted the experiments, analyzed the data, and wrote the manuscript. Y. L. and Y. W. were responsible for the software and writing-editing. M. L. assisted with the material synthesis and characterization. D. L. and Y. W. assisted with supervision and manuscript review. All authors contributed to the interpretation of the results.

Conflicts of interest

There are no conflicts to declare.

Acknowledgements

This work was supported by the National Natural Science Foundation of China (No. U24A20541, U24A20569 and 22278094), Guangdong Graduate Education Innovation Program (No. 2023JGXM_102), Jiangxi Province "Double Thousand Plan" (No. jxsq2023102142), Basic and Applied Basic Research Program of Guangzhou (No. SL2024A03J00499), and Guangdong Basic and Applied Basic Research Foundation (2025A1515010270).

Notes and references

1 J. Huang, Z. Wang, M. Hou, X. Dong, Y. Liu, Y. Wang and Y. Xia, *Nat. Commun.*, 2018, **9**, 2906.

2 J. Qi, Y. Tang, Z. Feng, J. Yan, G. Liu, M. Ye, W. Du, Q. Yang, Y. Wei, Y. Zhang, Z. Wen, X. Liu and C. C. Li, *Adv. Energy Mater.*, 2023, **14**, 2303616.

3 K. Yang, J. Ma, Y. Li, J. Jiao, S. Jiao, X. An, G. Zhong, L. Chen, Y. Jiang, Y. Liu, D. Zhang, J. Mi, J. Biao, B. Li, X. Cheng, S. Guo, Y. Ma, W. Hu, S. Wu, J. Zheng, M. Liu, Y.-B. He and F. Kang, *J. Am. Chem. Soc.*, 2024, **146**, 11371–11381.

4 Y. Song, M. Chen, Z. Zhong, Z. Liu, S. Liang and G. Fang, *Nat. Commun.*, 2025, **16**, 3142.

5 J. Li, Z. Guo, J. Wu, Z. Zheng, Z. Yu, F. She, L. Lai, H. Li, Y. Chen and L. Wei, *Adv. Energy Mater.*, 2023, **13**, 2301743.

6 N. Wang, X. Chen, H. Wan, B. Zhang, K. Guan, J. Yao, J. Ji, J. Li, Y. Gan, L. Lv, L. Tao, G. Ma, H. Wang, J. Zhang and H. Wang, *Adv. Funct. Mater.*, 2023, **33**, 2300795.

7 L. Ding, L. Wang, J. Gao, T. Yan, H. Li, J. Mao, F. Song, S. Fedotov, L. Y. Chang, N. Li, Y. Su, T. Liu and L. Zhang, *Adv. Funct. Mater.*, 2023, **33**, 2301648.

8 K. Zhu, L. Wu, C. Guo, J. Pu, Y. Liu, X. Chen, Y. Chen, P. Xue, J. Han and Y. Yao, *Adv. Funct. Mater.*, 2023, **33**, 2305098.

9 Y. Zhang, Y. Zhang, J. Deng, R. Xue, S. Yang, Y. Ma and Z. Wang, *Adv. Funct. Mater.*, 2023, **34**, 2310995.

10 J. Feng, X. Li, Y. Ouyang, H. Zhao, N. Li, K. Xi, J. Liang and S. Ding, *Angew. Chem., Int. Ed.*, 2024, **63**, e202407194.

11 F. Huang, X. Li, Y. Zhang, Y. Jie, X. Mu, C. Yang, W. Li, Y. Chen, Y. Liu, S. Wang, B. Ge, R. Cao, X. Ren, P. Yan, Q. Li, D. Xu and S. Jiao, *Adv. Mater.*, 2022, **34**, 2203710.

12 K. Zhu, J. Luo, D. Zhang, N. Wang, S. Pan, S. Zhou, Z. Zhang, G. Guo, P. Yang, Y. Fan, S. Hou, Z. Shao, S. Liu, L. Lin, P. Xue, G. Hong, Y. Yang and Y. Yao, *Adv. Mater.*, 2024, **36**, 2311082.

13 J. Zhang, Y. Liu, Y. Wang, Z. Zhu and Z. Yang, *Adv. Funct. Mater.*, 2024, **34**, 2401889.

14 B. Niu, Z. Li, D. Luo, X. Ma, Q. Yang, Y.-E. Liu, X. Yu, X. He, Y. Qiao and X. Wang, *Energy Environ. Sci.*, 2023, **16**, 1662–1675.

15 K. Zhao, G. Fan, J. Liu, F. Liu, J. Li, X. Zhou, Y. Ni, M. Yu, Y.-M. Zhang, H. Su, Q. Liu and F. Cheng, *J. Am. Chem. Soc.*, 2022, **144**, 11129–11137.

16 H. Lin, L. Zeng, C. Lin, J. Wu, H. He, C. Huang, W. Lai, P. Xiong, F. Xiao, Q. Qian, Q. Chen and J. Lu, *Energy Environ. Sci.*, 2025, **18**, 1282–1293.

17 K. Zhu, C. Guo, W. Gong, Q. Xiao, Y. Yao, K. Davey, Q. Wang, J. Mao, P. Xue and Z. Guo, *Energy Environ. Sci.*, 2023, **16**, 3612–3622.

18 W. Xu, J. Li, X. Liao, L. Zhang, X. Zhang, C. Liu, K. Amine, K. Zhao and J. Lu, *J. Am. Chem. Soc.*, 2023, **145**, 22456–22465.

19 S. Li, Y. Zhong, J. Huang, G. Lai, L. Li, L. Jiang, X. Xu, B. Lu, Y. Liu and J. Zhou, *Energy Environ. Sci.*, 2025, **18**, 2599–2609.

20 J. Hao, L. Yuan, Y. Zhu, M. Jaroniec and S. Z. Qiao, *Adv. Mater.*, 2022, **34**, 2206963.

21 M. Wu, X. Wang, F. Zhang, Q. Xiang, Y. Li and J. Guo, *Energy Environ. Sci.*, 2024, **17**, 619–629.

22 B. Hu, Y. Wang, X. Qian, W. Chen, G. Liang, J. Chen, J. Zhao, W. Li, T. Chen and J. Fu, *ACS Nano*, 2023, **17**, 12734–12746.

23 H. Peng, C. Wang, D. Wang, X. Song, C. Zhang and J. Yang, *Angew. Chem., Int. Ed.*, 2023, **62**, e202308068.

24 Q. Wu, J. Zhang, S. Yang, F. Luo, Z. Yan, X. Liu, H. Xie, J. Huang and Y. Chen, *Angew. Chem., Int. Ed.*, 2024, **64**, e202418524.

25 J. Hao, L. Yuan, C. Ye, D. Chao, K. Davey, Z. Guo and S. Z. Qiao, *Angew. Chem., Int. Ed.*, 2021, **60**, 7366–7375.

26 N. Chang, T. Li, R. Li, S. Wang, Y. Yin, H. Zhang and X. Li, *Energy Environ. Sci.*, 2020, **13**, 3527–3535.

27 D. Dong, T. Wang, Y. Sun, J. Fan and Y.-C. Lu, *Nat. Sustain.*, 2023, **6**, 1474–1484.

28 P. Wang, S. Liang, C. Chen, X. Xie, J. Chen, Z. Liu, Y. Tang, B. Lu and J. Zhou, *Adv. Mater.*, 2022, **34**, 2202733.

29 D. Xu, X. Ren, H. Li, Y. Zhou, S. Chai, Y. Chen, H. Li, L. Bai, Z. Chang, A. Pan and H. Zhou, *Angew. Chem., Int. Ed.*, 2024, **63**, e202402833.

30 L. Cao, D. Li, T. Pollard, T. Deng, B. Zhang, C. Yang, L. Chen, J. Vatamanu, E. Hu, M. J. Hourwitz, L. Ma, M. Ding, Q. Li, S. Hou, K. Gaskell, J. T. Fourkas, X.-Q. Yang, K. Xu, O. Borodin and C. Wang, *Nat. Nanotechnol.*, 2021, **16**, 902–910.

31 Z. Jiao, X. Cai, X. Wang, Y. Li, Z. Bie and W. Song, *Adv. Energy Mater.*, 2023, **13**, 2302676.

32 Q. Guo, G. Teri, W. Mo, J. Huang, F. Liu, M. Ye and D. Fu, *Energy Environ. Sci.*, 2024, **17**, 2888–2896.

33 Q. Li, A. Chen, D. Wang, Z. Pei and C. Zhi, *Joule*, 2022, **6**, 273–279.

34 H. Du, Y. Dong, Q. J. Li, R. Zhao, X. Qi, W. H. Kan, L. Suo, L. Qie, J. Li and Y. Huang, *Adv. Mater.*, 2023, **35**, 2210055.

35 H. Liu, Q. Ye, D. Lei, Z. Hou, W. Hua, Y. Huyan, N. Li, C. Wei, F. Kang and J.-G. Wang, *Energy Environ. Sci.*, 2023, **16**, 1610–1619.

36 L. Zhou, R. Yang, S. Xu, X. Lei, Y. Zheng, J. Wen, F. Zhang and Y. Tang, *Angew. Chem., Int. Ed.*, 2023, **62**, e202307880.

37 J. Luo, L. Xu, Y. Zhou, T. Yan, Y. Shao, D. Yang, L. Zhang, Z. Xia, T. Wang, L. Zhang, T. Cheng and Y. Shao, *Angew. Chem., Int. Ed.*, 2023, **62**, e202302302.

38 X. Yu, M. Chen, Z. Li, X. Tan, H. Zhang, J. Wang, Y. Tang, J. Xu, W. Yin, Y. Yang, D. Chao, F. Wang, Y. Zou, G. Feng, Y. Qiao, H. Zhou and S.-G. Sun, *J. Am. Chem. Soc.*, 2024, **146**, 17103–17113.

39 D. Xu, B. Chen, X. Ren, C. Han, Z. Chang, A. Pan and H. Zhou, *Energy Environ. Sci.*, 2024, **17**, 642–654.

40 G. Ma, L. Miao, Y. Dong, W. Yuan, X. Nie, S. Di, Y. Wang, L. Wang and N. Zhang, *Energy Storage Mater.*, 2022, **47**, 203–210.

41 Y. Zhang, S. Shen, K. Xi, P. Li, Z. Kang, J. Zhao, D. Yin, Y. Su, H. Zhao, G. He and S. Ding, *Angew. Chem., Int. Ed.*, 2024, **63**, e202407067.

42 X. Cao, W. Xu, D. Zheng, F. Wang, Y. Wang, X. Shi and X. Lu, *Angew. Chem., Int. Ed.*, 2024, **63**, e202317302.

43 K. Xie, K. Ren, Q. Wang, Y. Lin, F. Ma, C. Sun, Y. Li, X. Zhao and C. Lai, *eScience*, 2023, **3**, 100153.

44 S.-J. Guo, M.-Y. Yan, D.-M. Xu, P. He, K.-J. Yan, J.-X. Zhu, Y.-K. Yu, Z.-Y. Peng, Y.-Z. Luo and F.-F. Cao, *Energy Environ. Sci.*, 2025, **18**, 418–429.

45 Y. Yang, L. Qin, Q. He, C. Yin, Y. Lei, S. Liang and G. Fang, *Sci. Bull.*, 2025, **70**, 104–124.

46 F. Ming, Y. Zhu, G. Huang, A.-H. Emwas, H. Liang, Y. Cui and H. N. Alshareef, *J. Am. Chem. Soc.*, 2022, **144**, 7160–7170.

47 Y. Yang, G. Qu, H. Wei, Z. Wei, C. Liu, Y. Lin, X. Li, C. Han, C. Zhi and H. Li, *Adv. Energy Mater.*, 2023, **13**, 2203729.

48 Q. Zhang, Y. Ma, Y. Lu, L. Li, F. Wan, K. Zhang and J. Chen, *Nat. Commun.*, 2020, **11**, 4463.

49 L. Cao, D. Li, E. Hu, J. Xu, T. Deng, L. Ma, Y. Wang, X.-Q. Yang and C. Wang, *J. Am. Chem. Soc.*, 2020, **142**, 21404–21409.

50 M. Zhang, H. Hua, P. Dai, Z. He, L. Han, P. Tang, J. Yang, P. Lin, Y. Zhang, D. Zhan, J. Chen, Y. Qiao, C. C. Li, J. Zhao and Y. Yang, *Adv. Mater.*, 2023, **35**, 2208630.